ACSNANO

www.acsnano.org

ARTICLE

High-Performance Waveguide-Integrated Bi_2O_2Se Photodetector for Si Photonic Integrated Circuits

Jianghong Wu,[#] Maoliang Wei,[#] Jianglong Mu,[#] Hui Ma, Chuyu Zhong, Yuting Ye, Chunlei Sun, Bo Tang, Lichun Wang, Junying Li, Xiaomin Xu, Bilu Liu, Lan Li,* and Hongtao Lin*

Cite This: https://doi.org/10.1021/acsnano.1c04359

Read Online

ACCESS | Metrics & More | Article Recommendations | Supporting Information

ABSTRACT: Due to the excellent electrical and optical properties and their integration capability without lattice matching requirements, low-dimensional materials have received increasing attention in silicon photonic circuits. Bi_2O_2Se with high carrier mobility, narrow bandgap, and good air stability is very promising for high-performance near-infrared photodetectors. Here, the chemical vapor deposition method is applied to grow Bi_2O_2Se onto mica, and our developed polycarbonate/polydimethylsiloxane-assisted transfer method enables the clean and intact transfer of Bi_2O_2Se on top of a silicon waveguide. We demonstrated the Bi_2O_2Se/Si waveguide integrated photodetector with a small dark current of 72.9 nA, high responsivity of 3.5 $A{\cdot}W^{-1}$, fast rise/decay times of 22/78 ns, and low noise-equivalent power of 15.1 $pW{\cdot}Hz^{-0.5}$ at an applied voltage of 2 V in the O-band for transverse electric modes. Additionally, a microring resonator is designed for enhancing light−matter interaction, resulting in a wavelength-sensitive photodetector with reduced dark current (15.3 nA at 2 V) and more than a 3-fold enhancement in responsivity at the resonance wavelength, which is suitable for spectrally resolved applications. These results promote the integration of Bi_2O_2Se with a silicon photonic platform and are expected to accelerate the future use of integrated photodetectors in spectroscopy, sensing, and communication applications.

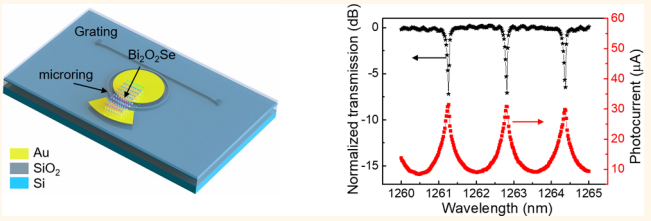

KEYWORDS: *Bi_2O_2Se, waveguide-integrated photodetector, silicon photonics, near-infrared, low-dimensional materials*

Near-infrared (NIR) photodetectors are a significant component for various applications such as optical communication, sensing, spectroscopy, and so on.[1−3] Over the past decade, atomically thin low-dimensional materials have drawn considerable attention for NIR photodetectors because of their excellent characteristics such as high carrier mobility, intriguing optical absorption, tunable optoelectronic parameters, and dangling-bond-free surface.[4−10] Recently, an air-stable material named Bi_2O_2Se, which can be obtained with high quality and large size by chemical vapor deposition (CVD) and vapor solid deposition, has been increasingly used in electronic and optoelectronic devices.[11−16] With an indirect bandgap of 0.8 eV and a high Hall mobility of ~29 000 $cm^2{\cdot}V^{-1}{\cdot}s^{-1}$ at 1.9 K,[17] Bi_2O_2Se has emerged as a promising material for NIR photodetectors.[18−21]

Up to now, free-space NIR photodetectors based on Bi_2O_2Se have already been reported. For instance, the Bi_2O_2Se-based phototransistor shows a broadband photoresponse ranging from 360 to 1800 nm.[22] Although this photodetector's responsivity is up to 22.12 $A{\cdot}W^{-1}$ at 1550 nm under the excitation of ultralow optical power (nW), its rise/decay times are 44/181 ms, limiting its application in high-speed detection. Heterostructures of Bi_2O_2Se with other low-dimensional materials have been constructed to optimize the performance. For example, a photodetector based on PbSe quantum dots/Bi_2O_2Se demonstrates a high responsivity at the wavelength of 2 μm.[23] PbSe quantum dots work as photoactive materials at 2 μm, while Bi_2O_2Se serves as the conductive channel. The photogating effect in such a device leads to a high responsivity but slow rise/decay times that are usually more than several seconds. Additionally, a photodetector based on WSe_2/Bi_2O_2Se heterostructure demonstrates a self-powered photovoltaic response with fast rise/decay times of 2.4/2.6 μs at 532 nm, but its responsivity is ultralow in the telewavelength range.[24]

Received: May 23, 2021
Accepted: October 12, 2021

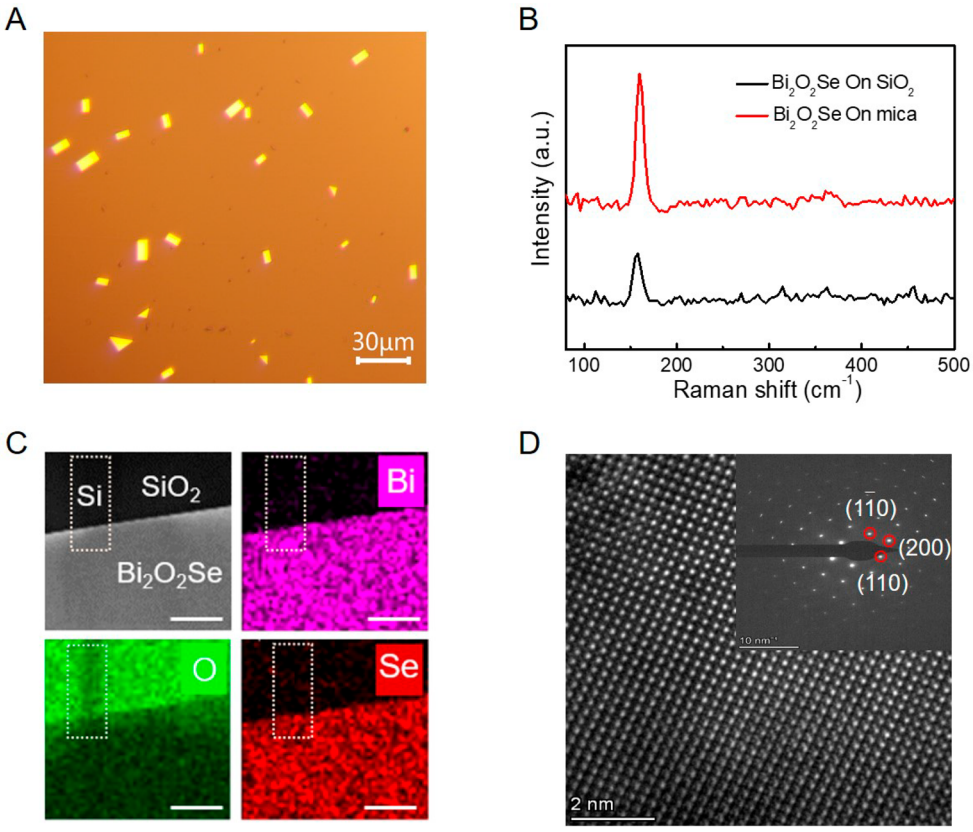

Figure 1. (A) Optical micrograph of Bi_2O_2Se flakes transferred onto PDMS. (B) Raman spectra of Bi_2O_2Se (about 100 nm thick) on mica and a SiO_2 substrate. (C) Scanning electron microscope (SEM) image of Bi_2O_2Se on SiO_2 substrate and its corresponding elemental maps analysis. Scale bar: 1 μm. (D) High-resolution transmission electron microscope (TEM) image of as-grown Bi_2O_2Se. The inset is the selected area electron diffraction (SAED) pattern of a Bi_2O_2Se flake.

The trade-off between the responsivity and rise/decay times in photodetectors can be overcome by a waveguide-integrated architecture, benefiting from the orthogonal directions in the path of photogenerated carriers and light propagation. Indeed, waveguide-integrated photodetectors not only possess the potential to achieve high-speed detection but also provide superior planar integration capability for on-chip applications. Moreover, a high signal-to-noise ratio could be achieved due to reduced detection volume compared with their free-space counterparts.[25] Among a wide variety of low-dimensional materials, graphene is the most commonly used material for waveguide-integrated photodetectors.[26−33] However, the characteristic of zero bandgap in graphene brings about a large dark current, low photocurrent-to-dark current ratio, and high noise in photodetectors. Therefore, low-dimensional semiconductors with a narrow bandgap such as black phosphorus (BP) and $MoTe_2$ are alternative candidates for Si waveguide-integrated photodetectors,[34−38] but the low stability of BP prevents it from constructing high-performance photodetectors in air. $MoTe_2$ is air-stable, but a bandgap of 1.04 eV leads to limited absorption when the operational wavelength is larger than 1.26 μm.[39−41] Given its air stability, high carrier mobility, and narrow bandgap, Bi_2O_2Se is attractive to be integrated with a Si waveguide to realize a high-performance NIR photodetector. However, there are currently no reports on the waveguide-integrated photodetector based on Bi_2O_2Se. Transferring Bi_2O_2Se from f-mica to a Si waveguide is one key point for obtaining a high-performance waveguide-integrated photodetector. At present, wet transfer with the assistance of a polymer film such as poly(methyl methacrylate) (PMMA) is the most common strategy to peel off Bi_2O_2Se from f-mica.[12,23] But this approach is cumbersome and not suitable for preparing a waveguide-integrated photodetector. On the contrary, the dry transfer process facilitates the alignment of low-dimensional materials with the underlying nanostructured waveguides.[42]

In this paper, we demonstrate both the waveguide-integrated and microring resonator (MRR)-integrated photodetectors based on Bi_2O_2Se. First, we synthesize Bi_2O_2Se on an f-mica substrate by the CVD method, and the dry transfer method assisted by polydimethylsiloxane (PDMS) or polycarbonate (PC)/PDMS is used to transfer Bi_2O_2Se from f-mica to the Si waveguide and MRR. Clean Bi_2O_2Se flakes are transferred on top of the Si waveguide, where light propagating in the waveguide can be evanescently coupled to Bi_2O_2Se. The waveguide-integrated photodetector shows a small dark current of 72.9 nA, high responsivity of 3.5 $A{\cdot}W^{-1}$, fast rise/decay times of 22/78 ns, and low noise-equivalent power (NEP) of 15.1 $pW{\cdot}Hz^{-0.5}$ at an applied voltage of 2 V in the O-band. The MRR-integrated photodetector shows a wavelength-sensitive photoresponse. The photocurrent increases about 3-fold at the resonance wavelength, which is induced by the enhanced light−matter interaction within the MRR structure. Owing to the thinner thickness and shorter length of Bi_2O_2Se that has been applied on the MRR, the MRR-integrated photodetector exhibits a reduced dark current (15.3 nA at 2 V) and comparable responsivity (1.83 $A{\cdot}W^{-1}$).

https://doi.org/10.1021/acsnano.1c04359
ACS Nano XXXX, XXX, XXX−XXX

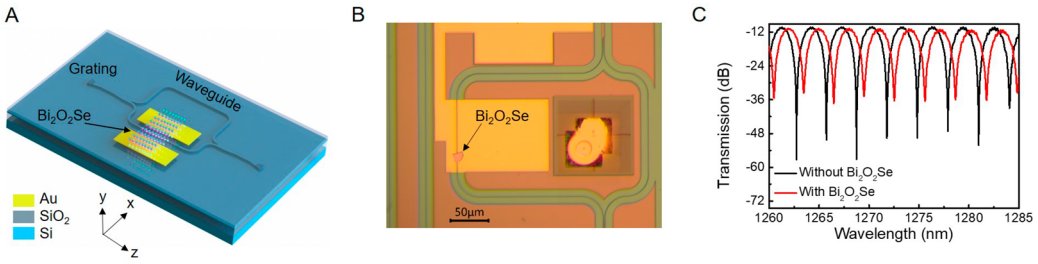

Figure 2. (A) Diagram of the waveguide-integrated Bi_2O_2Se photodetector. (B) Optical image of a typical integrated Bi_2O_2Se photodetector on an unbalanced MZI. (C) Transmission spectra of the unbalanced MZI with and without Bi_2O_2Se (73.6 nm thick).

RESULTS AND DISCUSSION

Bi_2O_2Se, possessing a layered structure, consists of covalently bonded $[Bi_2O_2]_n^{2n+}$ and $[Se]_n^{2n-}$ layers that stack alternately in a tetragonal unit cell with weak electrostatic force, which is similar to f-mica. We use f-mica as a substrate for growing Bi_2O_2Se in this work (see details in Methods). The size of the obtained Bi_2O_2Se flakes, with square or rectangular shapes, ranges from several microns to more than 20 μm. We transfer Bi_2O_2Se onto the SiO_2 substrate with the assistance of PDMS, and the optical micrograph of Bi_2O_2Se on PDMS is shown in Figure 1A, in which no cracks have been observed in Bi_2O_2Se. Raman spectra of Bi_2O_2Se on mica and a SiO_2 substrate are illustrated in Figure 1B, in which a characteristic A_{1g} peak at about 159 cm^{-1} is observed before and after transfer. The characteristic peak of f-mica is not shown due to the limited penetration depth of Raman light sources into a thick Bi_2O_2Se flake. The energy-dispersive X-ray spectroscopy (EDS) mappings of Bi_2O_2Se on a silicon-on-insulator (SOI) substrate (Figure 1C) reveal the uniform distribution of Bi, Se, and O elements. As for the image of O element distribution in Figure 1C, the SiO_2 substrate possesses a high percentage of O atoms compared with Bi_2O_2Se, leading to a bright color. A shallow dark line in the SiO_2 substrate is the bottom Si waveguide (Figure 1C). We transfer Bi_2O_2Se onto a Cu grid for TEM characterization. The high-magnification TEM image and the SAED pattern shown in Figure 1D demonstrate the single-crystal nature of our Bi_2O_2Se flakes. These measurements in Figure 1 indicate that the CVD-grown Bi_2O_2Se exhibits high quality, and the applied transfer methods do not damage the quality of Bi_2O_2Se.

The diagram of the waveguide-integrated Bi_2O_2Se photodetector is conceptually illustrated in Figure 2A, which consists of a couple of grating couplers, a single-mode waveguide, multimode interference (MMI), a pair of Au pads, and a Bi_2O_2Se flake. The grating couplers in our experiment only support TE (transverse electric) modes, and all results of optoelectronic response in this article correspond to TE modes as well. The passive optical devices are fabricated on 220 nm SOI wafers with multiproject wafer (MPW) processes involved, and the rib Si waveguide with a width of 397 nm and an etching depth of 151 nm (Figure S1) is planarized by backfilling with SiO_2 to protect Bi_2O_2Se from cracking at the edge of the Si waveguide. A pair of Au pads is located around one arm of an unbalanced Mach−Zehnder interferometer (MZI) with a suitable distance, avoiding optical loss and ensuring an effective collection of the photogenerated carriers. Bi_2O_2Se is well aligned to the gap between two Au pads on top of the waveguide by the PDMS-assisted transfer method. A detailed flowchart of the fabrication processes is illustrated in Figure S2. The optical image shown in Figure 2B represents a typical integrated photodetector where Bi_2O_2Se can absorb photons in the waveguide *via* evanescent coupling.

Optical absorption is a significant factor of photodetectors, which is affected by the thickness of photoactive materials and the degree of overlap between photoactive materials and the optical field. To determine the absorption coefficient of the Bi_2O_2Se/Si hybrid waveguide, we transfer Bi_2O_2Se onto one arm of the unbalanced MZI. As for devices based on the straight waveguide, the power difference between the output signal with and without photoactive materials is an approach to obtain the absorption coefficient. However, the practical coupling efficiency of the same grating coupler may be different in two operations, leading to a measurement error. This can be avoided by assessing the optical absorption information from analyzing the extinction ratio (ER) of the unbalanced MZI in the transmission spectra.[43] In an unbalanced MZI, a pair of MMIs works as a 3 dB beam splitter and combiner, respectively. Six serially cascaded MMIs (Figure S3A) are designed to better investigate and quantify the MMI's performance. The measured result shown in Figure S3B demonstrates that the beam splitter could equally allocate half of the input power to each output port of the 1 × 2 MMI. As shown in the inset of Figure S3B, the blue and red points are the measured power of two output ports of the sixth MMI. The two sets of data points overlap well, indicating the outstanding power equilibrium of the designed 1 × 2 MMI. The interference occurs when light passes through the beam combiner. Since the extinction ratio is more than 30 dB (before transferring Bi_2O_2Se), the propagation loss difference between the two arms could be neglected. Thereby the output power of an unbalanced MZI can be expressed as

$$P_{out} = \left(\frac{P_{in}}{4}\right)[e^{-\alpha l_1} + e^{-\alpha l_2} + 2e^{-\alpha(l_1+l_2)/2}\cos(2\pi n_{eff}\Delta L/\lambda)]$$

where P_{in} is the input power, α is the absorption coefficient of the Bi_2O_2Se/Si hybrid waveguide, and l_1 and l_2 are the lengths of the Bi_2O_2Se/Si hybrid waveguide on two arms, respectively. In our experiment, Bi_2O_2Se integrates with only one arm; thereby, l_2 is zero. ΔL is their length difference, λ is the wavelength of the incident light, and n_{eff} is the effective refractive index. Figure 2C shows the interferometric transmission spectra from which the peak position and ER of interference fringes of the unbalanced MZI are acquired accordingly. And there are apparent changes in both the ER and peak position upon the applying of Bi_2O_2Se on the MZI owing to its influence on optical absorption and the effective refractive index. In fact, the ER can be expressed as[43]

https://doi.org/10.1021/acsnano.1c04359
ACS Nano XXXX, XXX, XXX−XXX

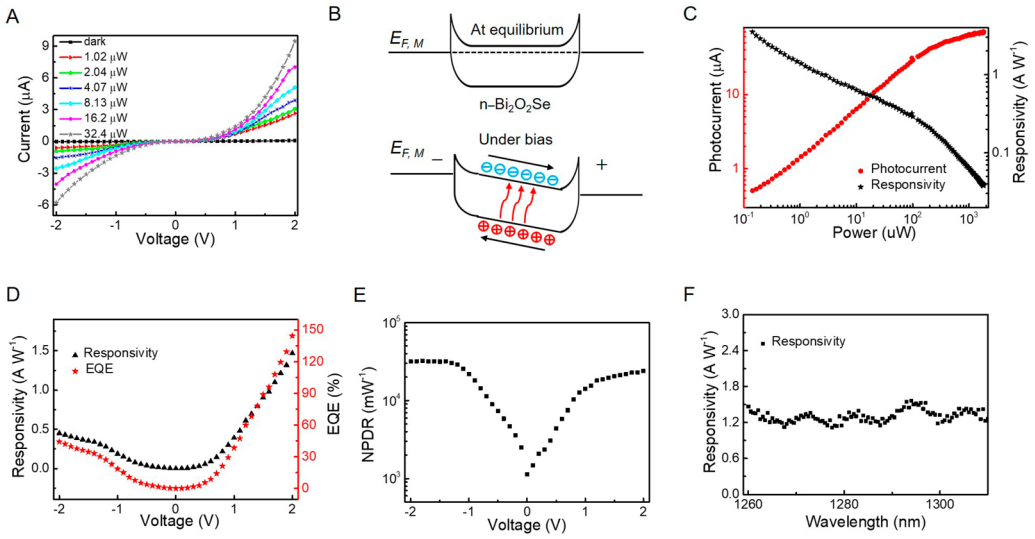

Figure 3. (A) Current−voltage (*IV*) curves of a Bi_2O_2Se photodetector in the dark and under illumination under different optical power at 1260 nm. (B) Energy band diagram of a Bi_2O_2Se photodetector at equilibrium, under illumination, and under an externally applied voltage. (C) Measured photocurrent (left-hand axis) and calculated responsivity (right-hand axis) of a Bi_2O_2Se photodetector under different optical power at 1260 nm at 2 V. (D) Calculated responsivity (left-hand axis) and external quantum efficiency (right-hand axis) of a Bi_2O_2Se photodetector under different applied voltages and an input power of 2.04 μW at 1260 nm. (E) Normalized photocurrent-to-dark-current ratio (NPDR) under different applied voltages and an input power of 2.04 μW at 1260 nm. (F) Spectral photoresponse of a Bi_2O_2Se photodetector at a wavelength ranging from 1260 to 1310 nm. The thickness of Bi_2O_2Se in the photodetector characterized is about 142.5 nm.

$$\mathrm{ER} = \frac{P_{\max}}{P_{\min}} = \frac{e^{-\alpha l_1} + 1 + 2e^{-\alpha l_1/2}}{e^{-\alpha l_1} + 1 - 2e^{-\alpha l_1/2}} = \left(\frac{1 + e^{-\alpha l_1/2}}{1 - e^{-\alpha l_1/2}}\right)^2$$

Thus the α of the Bi_2O_2Se/Si hybrid waveguide is calculated to be 0.07 dB/μm with the Bi_2O_2Se thickness of 73.6 nm. When the thickness of Bi_2O_2Se is 38.9 nm, the calculated α is about 0.03 dB/μm (Figure S4), indicating that designing a light-trapping structure to enhance optical absorption is necessary for a photodetector based on Bi_2O_2Se flakes. Furthermore, the SiO_2 layer being about 79.4 nm between Bi_2O_2Se and the Si waveguide degrades the α in our device, which is consistent with the results of the graphene/Si waveguide structure.[43]

The static photoresponse of the straight waveguide-integrated photodetectors based on Bi_2O_2Se with a thickness of 142.5 nm (Figure S5A) is characterized by a continuous wave laser, and the optical and SEM images of this photodetector are shown in Figure S6. Figure 3A illustrates the measured *IV* curves of an integrated photodetector under the applied voltage from −2 to 2 V in the dark and under illumination at the wavelength of 1260 nm. The dark current of this photodetector is about 72.9 nA at an applied voltage of 2 V. The current increases to 3.1 μA under illumination with an optical power of 2.04 μW, and the current rises gradually with the increasing optical power, indicating that Bi_2O_2Se is suitable for a photodetector in the O-band. The nonlinear behavior shown in the *IV* curves can be attributed to Schottky contact between Bi_2O_2Se and a metal. In our devices, Au pads are deposited on the flat substrate before the transfer of Bi_2O_2Se, which can reduce Fermi-level pinning and chemical disorder at the interface of Au and Bi_2O_2Se.[44] In this case, the Schottky barrier depends mainly on the work function of Au. The energy band diagram of the Au/Bi_2O_2Se/Au photodetector is shown in Figure 3B. The work function of Au is larger than the electron affinity of n-Bi_2O_2Se; thereby electrons in Bi_2O_2Se drift to Au and result in an upward energy band bending at the interface. This bending energy band suppresses the carrier transport and brings about a small dark current.

We then characterized the photoresponse under different optical power ranging from 0.14 to 1809.07 μW, and the measured photocurrent and calculated responsivity ($R = I_{ph}/P_{in}$) are shown in Figure 3C. I_{ph} and P_{in} are the photocurrent and input optical power launched into the photodetector, respectively. Responsivity decreases from 3.5 A·W^{-1} to 40 mA·W^{-1} when the optical power increases from 0.14 μW to 1809.07 μW. This nonlinear relationship between photocurrent and optical power probably results from trap states in Bi_2O_2Se, which leads to photocurrent gain under weak optical power. On the contrary, trap states are filled under high optical power, resulting in lower responsivity. We calculated the responsivity under the applied voltage ranging from −2 to 2 V, as shown in Figure 3D. The responsivity increases with the rising applied voltage, and it reaches up to 1.47 A·W^{-1} at an applied voltage of 2 V when the input power is 2.04 μW. The corresponding external quantum efficiency (EQE) can be calculated by EQE = $R \times hc/(q\lambda)$, where h, c, q, and λ are Planck's constant, the speed of light in a vacuum, elementary electron charge, and operational wavelength, respectively. EQE possesses the same tendency with responsivity, and it increases to 144.33% at an applied voltage of 2 V. This tendency may be attributed to the higher tunneling current induced by the lower barrier height of the Au/Bi_2O_2Se junction. And more efficient separation−collection of photoinduced carriers can be obtained at a larger applied voltage. The NPDR ((NPDR = $(I_p/I_d)/P_{in} = (I_p/P_{in})/I_d = R/I_d$) is estimated to be 3×10^4 mW^{-1} at the applied voltage of −2 V when the input power is 2.04 μW in Figure 3E, which is several orders of magnitude higher than that of graphene, BP, and even a Ge waveguide-integrated photodetector.[36,45,46] This high NPDR is attributed to both a small dark current and large responsivity, and it can be optimized through tuning the carrier concentration to a minimum by electrostatic doping. Some graphene photo-

https://doi.org/10.1021/acsnano.1c04359
ACS Nano XXXX, XXX, XXX−XXX

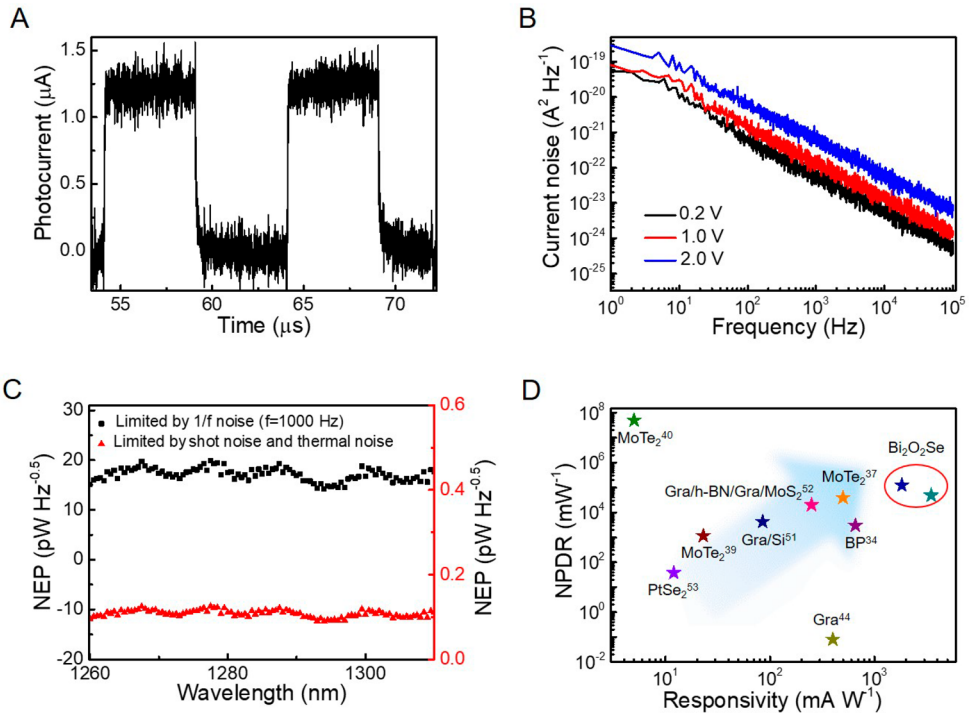

Figure 4. (A) Dynamic photoresponse of a Bi_2O_2Se photodetector under the excitation of the modulated laser at 1310 nm. (B) 1/*f* noise spectra of a Bi_2O_2Se photodetector under different applied voltages. (C) Spectral noise-equivalent power (NEP) at a wavelength ranging from 1260 to 1310 nm under an applied voltage of 2 V; left-hand axis corresponds to the calculated NEP limited by 1/*f* noise, and the right-hand axis corresponds to the calculated NEP limited by shot and thermal noise. (D) Summary of the device performance for some waveguide-integrated photodetectors based on low-dimensional materials. The blue arrow represents the better performance. The thickness of Bi_2O_2Se in the photodetector is about 142.5 nm.

detectors possess zero dark current in the self-driven mode, but responsivity is weak in this situation. Therefore, the Bi_2O_2Se photodetector shows obvious advantages in terms of both responsivity and dark current.

We measured the spectral photoresponse as well, and the corresponding results are illustrated in Figure 3F. The responsivity fluctuates slightly when the wavelength increases from 1260 nm to 1310 nm, which can be attributed to the smaller gain at larger optical power and more efficient photon-to-electron transition at shorter wavelengths in the O-band considering Bi_2O_2Se's indirect bandgap of 0.8 eV.[47] At a wavelength of 1330 nm, the responsivity of the proposed photodetector is 1.75 $A{\cdot}W^{-1}$. In our design, the adopted grating couplers have limited operation optical bandwidth. Taking advantage of the edge coupling method, we can replace the grating couplers with end-face coupling waveguides to ensure the functionality of the Bi_2O_2Se-based photodetector with a broader optical bandwidth.

The dynamic response (Figure 4A) is measured under the excitation of the modulated laser, and a magnified plot of one response cycle is shown in (Figure S7). The rise and decay times are 22 and 78 ns, respectively, benefiting from the fast carrier mobility of Bi_2O_2Se and the short channel length between two Au pads. Furthermore, the noise-equivalent power (NEP) characterizing the detection limit is another significant parameter for a photodetector. The total current noise of a photodetector mainly includes the 1/*f* noise, shot noise, and thermal noise. Hooge's empirical relationship is usually used for analyzing 1/*f* noise, which can be expressed as[48] $S_i = Ai^{\alpha}/f^{\beta}$, where *i*, *f*, and *A* are the channel current, the frequency, and noise amplitude, respectively. Figure 4B is the measured 1/*f* noise spectral density, demonstrating that our photodetectors possess typical characteristics of 1/*f* noise. The measured 1/*f* noise decreases from 2.9×10^{-19} $A^2{\cdot}Hz^{-1}$ at a frequency of 1 Hz to $5.6 \times 10^{-24}A^2{\cdot}Hz^{-1}$ at 100 kHz at an applied voltage of 2.0 V. A higher external applied voltage brings about an optimal responsivity but leads to a higher 1/*f* noise. The shot noise can be expressed as $S_s = 2qi_d\Delta f$,[49] where i_d and Δf are the dark current and bandwidth, respectively. The dark current of the proposed Bi_2O_2Se-based waveguide-integrated photodetector is 72.9 nA at an applied voltage of 2 V, and the calculated shot noise is 2.3×10^{-26} $A^2{\cdot}Hz^{-1}$. The thermal noise is calculated to be 6.0×10^{-28} $A^2{\cdot}Hz^{-1}$ by $S_t = 4kT\Delta f/R_s$,[49] where *k*, *t*, and R_s are the Boltzmann constant, the temperature (about 300 K in our experiment), and the device's resistance. Therefore, 1/*f* noise is the main noise at low frequency, and the NEP is estimated to be 15.1 $pW{\cdot}Hz^{-0.5}$ at a frequency and wavelength of 1000 Hz and 1260 nm, respectively. On the contrary, the shot noise is dominant at a higher frequency, and NEP is estimated to be 0.1 $pW{\cdot}Hz^{-0.5}$. The spectral NEP at the wavelength ranging from 1260 to 1310 nm is shown in Figure 4C, indicating a small detectable power within this wavelength range.

As shown in Figure 4D, we list several reported waveguide-integrated photodetectors based on low-dimensional materials.[34,37,39,40,50−53] The proposed photodetector based on Bi_2O_2Se not only possesses a low dark current but also has high responsivity at the O band, exhibiting potential applications in the fields of spectroscopy, sensing, and communication as high-performance photodetectors integrated onto silicon photonic platforms.

https://doi.org/10.1021/acsnano.1c04359
ACS Nano XXXX, XXX, XXX−XXX

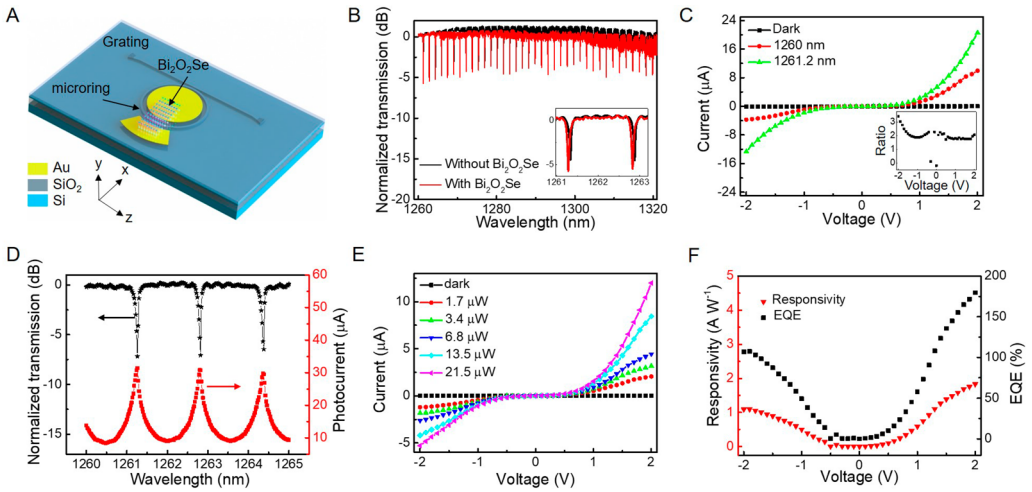

Figure 5. (A) Schematic of the MRR-enhanced photodetector showing Bi_2O_2Se integrated with a planarized microring. (B) Transmission spectra of the MRR with and without Bi_2O_2Se. Inset: Zoom-in of the spectra. (C) Photocurrent at resonance and off-resonance wavelength. The inset is the photocurrent ratio at resonance and off-resonance wavelength. (D) Spectral response of the Bi_2O_2Se-based MRR-enhanced photodetector. (E) *IV* curves of the Bi_2O_2Se-based MRR-enhanced photodetector in the dark and under illumination with different optical power at resonance wavelength. (F) Calculated responsivity (left-hand axis) and external quantum efficiency (right-hand axis) of a Bi_2O_2Se photodetector under different applied voltages and an optical power of 0.86 μW. The thickness of Bi_2O_2Se in the photodetector is about 63 nm.

Furthermore, Bi_2O_2Se is applied onto a silicon MRR to achieve a high-performance integrated photodetector. On the one hand, the enhanced light−matter interaction by a MRR makes it possible to realize quantum efficiency comparable to a thicker and longer Bi_2O_2Se photodetector on the straight waveguide.[37,54,55] On the other hand, such a cavity-enhanced photodetector is wavelength sensitive, which plays an important role in spectrally resolved applications such as wavelength division multiplexing systems.[56,57] Figure 5A is a schematic of the MRR-enhanced photodetector, indicating a pair of Au pads close to the MRR and Bi_2O_2Se on top of the Au pads and the MRR. Furthermore, FIB-SEM of this photodetector is shown in Figure S1B,C. Typical transmission spectra of an MRR are shown inFigure 5B. The transmission spectra of an MRR with different gaps (from 200 to 400 nm) are measured (Figure S8A), from which the gap under the critical coupling condition is confirmed to be less than 300 nm. The cavity loss increases after introducing Bi_2O_2Se, so it is difficult to observe the resonance peak in the spectra of the Bi_2O_2Se photodetector integrated with an undercoupled MRR (Figure S8B). Thereby, overcoupled MRRs are used to ensure resonance peaks with high extinctions upon applying Bi_2O_2Se onto a silicon MRR. We choose the MRR with a gap of 200 nm for the photodetector, and the corresponding transmission spectra without and with Bi_2O_2Se are shown in Figure 5B. The quality factor of the MRR decreases from 3.5×10^4 to 2.4×10^4, which can be attributed to the additional optical loss that Bi_2O_2Se brings to the cavity. And for the MRR with Bi_2O_2Se, the number of times that a resonance photon passes through the cavity is calculated to be 754 (the detailed process is shown in Supporting Information 9), and the photon circulation brings about an enhanced photocurrent at resonance wavelength. The thickness of the Bi_2O_2Se flake in this photodetector is about 63.0 nm (Figure S5B), and the optical and SEM images of this photodetector are shown in Figure S6. Moreover, the *n* value of Bi_2O_2Se is estimated to be 4.079 from the resonance peak shift after transferring Bi_2O_2Se, and the simulated modal intensity for fundamental TE modes in the Bi_2O_2Se/Si waveguide is shown in Figure S9. Shown in Figure 5C are the *IV* curves of the photodetector at resonance and off-resonance wavelength. The inset is the ratio between current at resonance and off-resonance wavelengths, indicating a maximum enhancement of 3.4 (at an applied voltage of −2 V) in photocurrent at resonance wavelength. This photodetector shows a 5-fold decrease in the dark current (15.3 nA@2 V) compared with the straight waveguide-integrated photodetector, which is partially attributed to the thinner thickness. The spectral response of the MRR-enhanced photodetector at a wavelength ranging from 1260 to 1265 nm is shown in Figure 5D, where the wavelength-variation photoresponse is observed, and the maximum photocurrent is achieved at the resonance wavelength at an applied voltage of 2 V. The photocurrent exhibits more than a 3-fold enhancement at resonance wavelength, comparing with that at off-resonance wavelength. *IV* curves of an MRR-enhanced photodetector under different power at the resonance wavelength are shown in Figure 5E. The current increases gradually with the increasing optical power. The calculated responsivity and EQE at different applied voltage are shown in Figure 5F. And a responsivity of 1.83 $A \cdot W^{-1}$ and EQE of 179.6% at the resonance wavelength (at an applied voltage of 2 V) are obtained. All in all, this MRR-enhanced photodetector shows an advantage for optimizing a photodetector, and the wavelength-sensitive characteristics have the potential in a wavelength division multiplexing system for on-chip spectroscopy, sensing, and communication applications.

CONCLUSIONS

In conclusion, we demonstrated the silicon waveguide and MRR-integrated Bi_2O_2Se photodetectors operating in the O-band. Bi_2O_2Se interacts with the light propagating along the waveguide through evanescent field coupling in this type of photodetector. The optical absorption of the Bi_2O_2Se/Si hybrid waveguide is measured by an unbalanced Mach−Zehnder interferometer. As a result, we showed its broadband operation capability in the O-band with a responsivity of 3.5 A·

https://doi.org/10.1021/acsnano.1c04359
ACS Nano XXXX, XXX, XXX−XXX

W^{-1} at 1260 nm and an applied voltage of 2 V, a dark current of 72.9 nA, and rise/decay times of 22/78 ns, respectively. Moreover, we also analyzed noise characteristics and found that $1/f$ noise is the dominant noise when the frequency is below 10^5 Hz, and the corresponding NEP is about 15.1 pW $Hz^{-0.5}$. The photodetection is further enhanced by integrating Bi_2O_2Se with MRR cavities to increase the optical absorption. The MRR-enhanced photodetector shows a 3-fold improvement in photocurrent at the resonance wavelength comparing with that at the off-resonance wavelength, suitable for devices with a small volume of photoactive materials. These results promote the integration of Bi_2O_2Se photodetectors on a silicon photonic platform and hold great promise for extensive applications in spectroscopy, sensing, and communication.

METHODS

Synthesis of Bi_2O_2Se. Bi_2O_2Se nanoflakes were grown by low-pressure CVD (LPCVD) processes in the one-inch diameter quartz tube (length of 120 cm) located inside a horizontal furnace. A specific mass ratio of Bi_2O_3 (purchased from Macklin, 99.99%) and Bi_2Se_3 (purchased from Aladdin, 99.99%) as reaction precursors was put into two quartz boats, respectively. Bi_2O_3 powder was sited at the hot center of the furnace, while Bi_2Se_3 powder was placed upstream at a distance of 10 cm, and the freshly cleaved mica substrates (1 cm × 1 cm) were placed at 10−12 cm downstream. The quartz tube was evacuated using a mechanical pump in all growth processes to avoid the ambient environment. High-purity argon (Ar) was used as the carrier gas to transport precursors' vapor from upstream to downstream. The furnace was heated to the goal temperature of 700 °C with a heating rate of 30−35 °C·min^{-1} and kept for 1−10 min. Meanwhile, the flow rate of Ar was 200 standard cubic centimeters per minute (sccm), and the growth pressure in the quartz tube was about 2 Torr. Finally, the furnace cooled naturally to ambient temperature.

Materials Characterization and Transfer. Raman spectra (WITec, Alpha300R), AFM (Oxford Instruments, Cypher ES), TEM (Thermo Fisher Scientific, Talos F200X G2), and SEM (Hitachi, Regulus 8230) were used to evaluate the quality and characteristics of the obtained Bi_2O_2Se. The flexible PDMS was attached and pressed to make a strong adhesion between Bi_2O_2Se flakes and PDMS. Next, PDMS along with Bi_2O_2Se was peeled off from the f-mica with the help of the water droplet (5−10 μL). After that, Bi_2O_2Se was aligned with the Au electrode and waveguide under a microscope, and PDMS was removed after pressing Bi_2O_2Se onto the Au electrode and being heated for 10 min (60 °C). Finally, Bi_2O_2Se was transferred onto the Au electrode upon the removal of PDMS. However, there were still lots of Bi_2O_2Se flakes on the f-mica after repeating these steps several times, but PMDS-assisted transfer was not efficient enough at this stage. We proposed a PC-assisted approach to peel off Bi_2O_2Se from the f-mica more efficiently. PC (dissolved in chloroform) was dissolved in chloroform (PC/chloroform = 6/94) to obtain a transparent solution. This transparent solution was spin-coated onto the surface of the mica that was fixed on a glass slide, which was heated for 60 s (90 °C). With the assistance of a water droplet (5−10 μL), PC along with Bi_2O_2Se could be peeled off from f-mica, and this exploited PC film was fixed on a blue tape. Afterward, PDMS was attached and pressed onto PC, transferring Bi_2O_2Se from PC to PDMS. The next step was the same as the PDMS-assisted transfer.

Device Fabrication. The passive Si photonic devices were fabricated with standard 220-nm-SOI MPW processes in IMECAS. On top of the device is the buried SiO_2 layer with a 2 μm thickness, which was chemically and mechanically polished to a flat surface. Metal pads in the devices were patterned by electron-beam lithography (Raith, Voyager) followed by deposition of metal pads (Ti/Au, 5/50 nm) by electron-beam evaporation (ULvac Vacuum Technology (Suzhou) Co., Ltd., Ei-5Z) and a standard lift-off process. After depositing the metal pads, Bi_2O_2Se was transferred with the help of a PC/PDMS film.

Device Measurement. Electrical measurements were collected by a semiconductor analyzer (PDA, FS-Pro). Static photoresponse measurements (Figure S10) were done under the excitation of a tunable semiconductor laser (Santec Corporation, TSL-550) with tunable wavelength ranging from 1260 to 1620 nm. A variable optical attenuator (Thorlab, V1550A) was used to tune the power of the incident light. A polarization controller was applied to tune the polarization of the incident light and improve the coupling efficiency of the grating coupler. Dynamic photoresponse measurements (Figure S11) were under the excitation of a modulated laser (1310 nm) driven by a signal generator (SDG6032X-E), and the output signal was obtained by an oscilloscope (SDS5104X).

ASSOCIATED CONTENT

Supporting Information

The Supporting Information is available free of charge at https://pubs.acs.org/doi/10.1021/acsnano.1c04359.

Cross-section SEM images of the rib waveguide and Bi_2O_2Se photodetector; detailed flowchart of the fabrication processes; optical image and optical performance of cascading MMIs; optical absorption of Bi_2O_2Se; thickness of Bi_2O_2Se; optical and SEM images for photodetectors; dynamic optoelectronic response of the Bi_2O_2Se photodetector; transmission spectra of the microring resonator; the relationship between performance enhancement and the cavity Q; the simulated modal intensity for the Bi_2O_2Se photodetector; static photoresponse measurement setup; dynamic photoresponse measurement setup (PDF)

AUTHOR INFORMATION

Corresponding Authors

Hongtao Lin − *State Key Laboratory of Modern Optical Instrumentation, College of Information Science and Electronic Engineering, Zhejiang University, Hangzhou 310027, China;* orcid.org/0000-0001-7432-3644; Email: hometown@zju.edu.cn

Lan Li − *Key Laboratory of 3D Micro/Nano Fabrication and Characterization of Zhejiang Province, School of Engineering, Westlake University, Hangzhou 310024, China; Institute of Advanced Technology, Westlake Institute for Advanced Study, Hangzhou 310024, China;* orcid.org/0000-0002-9097-9157; Email: lilan@westlake.edu.cn

Authors

Jianghong Wu − *State Key Laboratory of Modern Optical Instrumentation, College of Information Science and Electronic Engineering, Zhejiang University, Hangzhou 310027, China; Key Laboratory of 3D Micro/Nano Fabrication and Characterization of Zhejiang Province, School of Engineering, Westlake University, Hangzhou 310024, China; Institute of Advanced Technology, Westlake Institute for Advanced Study, Hangzhou 310024, China*

Maoliang Wei − *State Key Laboratory of Modern Optical Instrumentation, College of Information Science and Electronic Engineering, Zhejiang University, Hangzhou 310027, China*

Jianglong Mu − *Shenzhen Geim Graphene Center, Tsinghua-Berkeley Shenzhen Institute and Tsinghua Shenzhen International Graduate School, Tsinghua University, Shenzhen, Guangdong 518055, China*

https://doi.org/10.1021/acsnano.1c04359
ACS Nano XXXX, XXX, XXX−XXX

Hui Ma − *State Key Laboratory of Modern Optical Instrumentation, College of Information Science and Electronic Engineering, Zhejiang University, Hangzhou 310027, China*
Chuyu Zhong − *State Key Laboratory of Modern Optical Instrumentation, College of Information Science and Electronic Engineering, Zhejiang University, Hangzhou 310027, China*
Yuting Ye − *Key Laboratory of 3D Micro/Nano Fabrication and Characterization of Zhejiang Province, School of Engineering, Westlake University, Hangzhou 310024, China; Institute of Advanced Technology, Westlake Institute for Advanced Study, Hangzhou 310024, China*
Chunlei Sun − *Key Laboratory of 3D Micro/Nano Fabrication and Characterization of Zhejiang Province, School of Engineering, Westlake University, Hangzhou 310024, China; Institute of Advanced Technology, Westlake Institute for Advanced Study, Hangzhou 310024, China*
Bo Tang − *Institute of Microelectronics, Chinese Academic Society, Beijing 100029, China*
Lichun Wang − *State Key Laboratory of Modern Optical Instrumentation, College of Information Science and Electronic Engineering, Zhejiang University, Hangzhou 310027, China*
Junying Li − *State Key Laboratory of Modern Optical Instrumentation, College of Information Science and Electronic Engineering, Zhejiang University, Hangzhou 310027, China*
Xiaomin Xu − *Shenzhen Geim Graphene Center, Tsinghua-Berkeley Shenzhen Institute and Tsinghua Shenzhen International Graduate School, Tsinghua University, Shenzhen, Guangdong 518055, China*
Bilu Liu − *Shenzhen Geim Graphene Center, Tsinghua-Berkeley Shenzhen Institute and Tsinghua Shenzhen International Graduate School, Tsinghua University, Shenzhen, Guangdong 518055, China;* orcid.org/0000-0002-7274-5752

Complete contact information is available at: https://pubs.acs.org/10.1021/acsnano.1c04359

Author Contributions

H.L., L.L, and J.W. conceived the project. X.X., B.L., and J.M. grew Bi_2O_2Se. J.W., M.W., H.M., C.Z., Y.Y., L.W., J.L., L.W., and B.T. fabricated these devices. C.S. and M.W. designed the passive optical devices. J.W. performed optical and optoelectronic measurements. H.L., L.L, and J.W. analyzed the data and wrote the manuscript. All authors commented on the manuscript.

Author Contributions

#J.W., M.W., and J.M. contributed equally to this work.

Notes

The authors declare no competing financial interest.

ACKNOWLEDGMENTS

The research was partially supported by the National Key Research and Development Program of China (2019YFB2203003), National Natural Science Foundation of China (Grant Numbers 61975179 and 91950204), Open Fund of the State Key Laboratory of Integrated Optoelectronics (Grant Number IOSKL2020KF05), the Fundamental Research Funds for the Central Universities (Grant Numbers 2020XZZX005-07 and 2021QNA5007), Leading Innovative and Entrepreneur Team Introduction Program of Zhejiang (Grant Number 2020R01005), the start-up fund of Westlake University, and the Foundation of Key Laboratory of 3D Micro/Nano Fabrication and Characterization of Zhejiang Province, Westlake University. The authors thank the ZJU Micro-Nano Fabrication Center at Zhejiang University, Westlake Center for Micro/Nano Fabrication and Instrumentation, and Service Center for Physical Sciences and Molecular Sciences at Westlake University for the facility support.

REFERENCES

(1) Atabaki, A. H.; Moazeni, S.; Pavanello, F.; Gevorgyan, H.; Notaros, J.; Alloatti, L.; Wade, M. T.; Sun, C.; Kruger, S. A.; Meng, H. Y.; Al Qubaisi, K.; Wang, I.; Zhang, B. H.; Khilo, A.; Baiocco, C. V.; Popovic, M. A.; Stojanovic, V. M.; Ram, R. J. Integrating Photonics with Silicon Nanoelectronics for the Next Generation of Systems on a Chip. *Nature* **2018**, *556*, 349−354.
(2) Lin, H. T.; Luo, Z. Q.; Gu, T.; Kimerling, L. C.; Wada, K.; Agarwal, A.; Hu, J. J. Mid-Infrared Integrated Photonics on Silicon: A Perspective. *Nanophotonics* **2017**, *7*, 393−420.
(3) Yuan, S.; Naveh, D.; Watanabe, K.; Taniguchi, T.; Xia, F. A Wavelength-Scale Black Phosphorus Spectrometer. *Nat. Photonics* **2021**, *15*, 601−607.
(4) Lan, C. Y.; Shi, Z.; Cao, R.; Li, C.; Zhang, H. 2D Materials beyond Graphene toward Si Integrated Infrared Optoelectronic Devices. *Nanoscale* **2020**, *12*, 11784−11807.
(5) Mak, K. F.; Ju, L.; Wang, F.; Heinz, T. F. Optical spectroscopy of Graphene: From the far Infrared to the Ultraviolet. *Solid State Commun.* **2012**, *152*, 1341−1349.
(6) Novoselov, K. S.; Geim, A. K.; Morozov, S. V.; Jiang, D.; Zhang, Y.; Dubonos, S. V.; Grigorieva, I. V.; Firsov, A. A. Electric Field Effect in Atomically Thin Carbon Films. *Science* **2004**, *306*, 666−669.
(7) Singh, A.; Jo, S. S.; Li, Y. F.; Wu, C. M.; Li, M.; Jaramillo, R. Refractive Uses of Layered and Two-Dimensional Materials for Integrated Photonics. *ACS Photonics* **2020**, *7*, 5270−5285.
(8) Ma, Q. J.; Ren, G. H.; Mitchell, A.; Ou, J. Z. Recent Advances on Hybrid Integration of 2D Materials on Integrated Optics Platforms. *Nanophotonics* **2020**, *9*, 2191−2214.
(9) Wang, Q.; Zhou, C. J.; Chai, Y. Breaking Symmetry in Device Design for Self-Driven 2D Material Based Photodetectors. *Nanoscale* **2020**, *12*, 8109−8118.
(10) Zhong, C.; Li, J.; Lin, H. Graphene-Based All-Optical Modulators. *Frontiers of Optoelectronics* **2020**, *13*, 114−128.
(11) Yang, C. M.; Chen, T. C.; Verma, D.; Li, L. J.; Liu, B.; Chang, W. H.; Lai, C. S. Bidirectional All-Optical Synapses Based on a 2D Bi_2O_2Se/Graphene Hybrid Structure for Multifunctional Optoelectronics. *Adv. Funct. Mater.* **2020**, *30*, 2001598.
(12) Khan, U.; Luo, Y. T.; Tang, L.; Teng, C. J.; Liu, J. M.; Liu, B. L.; Cheng, H. M. Controlled Vapor Solid Deposition of Millimeter-Size Single Crystal 2D Bi_2O_2Se for High-Performance Phototransistors. *Adv. Funct. Mater.* **2019**, *29*, 1807979.
(13) Quhe, R. G.; Liu, J. C.; Wu, J. X.; Yang, J.; Wang, Y. Y.; Li, Q. H.; Li, T. R.; Guo, Y.; Yang, J. B.; Peng, H. L.; Lei, M.; Lu, J. High-Performance Sub-10 nm Monolayer Bi_2O_2Se Transistors. *Nanoscale* **2019**, *11*, 532−540.
(14) Yang, H.; Tan, C. W.; Deng, C. Y.; Zhang, R. Y.; Zheng, X. M.; Zhang, X. Z.; Hu, Y. Z.; Guo, X. X.; Wang, G.; Jiang, T.; Zhang, Y.; Peng, G.; Peng, H. L.; Zhang, X. A.; Qin, S. A. Bolometric Effect in Bi_2O_2Se Photodetectors. *Small* **2019**, *15*, 1904482.
(15) Tan, C. W.; Tang, M.; Wu, J. X.; Liu, Y. N.; Li, T. R.; Liang, Y.; Deng, B.; Tan, Z. J.; Tu, T.; Zhang, Y. C.; Liu, C.; Chen, J. H.; Wang, Y.; Peng, H. L. Wafer-Scale Growth of Single-Crystal 2D Semiconductor on Perovskite Oxides for High-Performance Transistors. *Nano Lett.* **2019**, *19*, 2148−2153.
(16) Wang, J. L.; Wu, J.; Wang, T.; Xu, Z. K.; Wu, J. F.; Hu, W. H.; Ren, Z.; Liu, S.; Behnia, K.; Lin, X. T-Square Resistivity without Umklapp Scattering in Dilute Metallic Bi_2O_2Se. *Nat. Commun.* **2020**, *11*, 3486.

(17) Wu, J. X.; Yuan, H. T.; Meng, M. M.; Chen, C.; Sun, Y.; Chen, Z. Y.; Dang, W. H.; Tan, C. W.; Liu, Y. J.; Yin, J. B.; Zhou, Y. B.; Huang, S. Y.; Xu, H. Q.; Cui, Y.; Hwang, H. Y.; Liu, Z. F.; Chen, Y. L.; Yan, B. H.; Peng, H. L. High Electron Mobility and Quantum Oscillations in Non-Encapsulated Ultrathin Semiconducting Bi_2O_2Se. *Nat. Nanotechnol.* **2017**, *12*, 530−534.
(18) Sun, Y.; Zhang, J.; Ye, S.; Song, J.; Qu, J. L. Progress Report on Property, Preparation, and Application of Bi_2O_2Se. *Adv. Funct. Mater.* **2020**, *30*, 2004480.
(19) Liu, X. L.; Li, R. P.; Hong, C. Y.; Huang, G. F.; Pan, D. F.; Ni, Z. H.; Huang, Y. Q.; Ren, X. M.; Cheng, Y. C.; Huang, W. Highly Efficient Broadband Photodetectors Based on Lithography-Free Au/Bi_2O_2Se/Au heterostructures. *Nanoscale* **2019**, *11*, 20707−20714.
(20) Liu, X.; Wang, W. H.; Yang, F.; Feng, S. P.; Hu, Z. L.; Lu, J. P.; Ni, Z. H. Bi_2O_2Se/BP van der Waals Heterojunction for High Performance Broadband Photodetector. *Sci. China-Inf. Sci.* **2021**, *64*, 140404.
(21) Hong, C. Y.; Tao, Y.; Nie, A. M.; Zhang, M. H.; Wang, N.; Li, R. P.; Huang, J. Q.; Huang, Y. Q.; Ren, X. M.; Cheng, Y. C.; Liu, X. L. Inclined Ultrathin Bi_2O_2Se Films: A Building Block for Functional van der Waals Heterostructures. *ACS Nano* **2020**, *14*, 16803−16812.
(22) Tong, T.; Chen, Y. F.; Qin, S. C.; Li, W. S.; Zhang, J. R.; Zhu, C. H.; Zhang, C. C.; Yuan, X.; Chen, X. Q.; Nie, Z. H.; Wang, X. R.; Hu, W. D.; Wang, F. Q.; Liu, W. Q.; Wang, P.; Wang, X. F.; Zhang, R.; Xu, Y. B. Sensitive and Ultrabroadband Phototransistor Based on Two-Dimensional Bi_2O_2Se Nanosheets. *Adv. Funct. Mater.* **2019**, *29*, 1905806.
(23) Luo, P.; Zhuge, F. W.; Wang, F. K.; Lian, L. Y.; Liu, K. L.; Zhang, J. B.; Zhai, T. Y. PbSe Quantum Dots Sensitized High-Mobility Bi_2O_2Se Nanosheets for High-Performance and Broadband Photodetection beyond 2 μm. *ACS Nano* **2019**, *13*, 9028−9037.
(24) Luo, P.; Wang, F. K.; Qu, J. Y.; Liu, K. L.; Hu, X. Z.; Liu, K. W.; Zhai, T. Y. Self-Driven WSe_2/Bi_2O_2Se van der Waals Heterostructure Photodetectors with High Light On/Off Ratio and Fast Response. *Adv. Funct. Mater.* **2021**, *31*, 2008351.
(25) Wu, J.; Ma, H.; Yin, P.; Ge, Y.; Zhang, Y.; Li, L.; Zhang, H.; Lin, H. Two-Dimensional Materials for Integrated Photonics: Recent Advances and Future Challenges. *Small Sci.* **2021**, *1*, 2000053.
(26) Shiue, R. J.; Gao, Y. D.; Wang, Y. F.; Peng, C.; Robertson, A. D.; Efetov, D. K.; Assefa, S.; Koppens, F. H. L.; Hone, J.; Englund, D. High-Responsivity Graphene-Boron Nitride Photodetector and Autocorrelator in a Silicon Photonic Integrated Circuit. *Nano Lett.* **2015**, *15*, 7288−7293.
(27) Wang, J. Q.; Cheng, Z. Z.; Chen, Z. F.; Wan, X.; Zhu, B. Q.; Tsang, H. K.; Shu, C.; Xu, J. B. High-Responsivity Graphene-on-Silicon Slot Waveguide Photodetectors. *Nanoscale* **2016**, *8*, 13206−13211.
(28) Pospischil, A.; Humer, M.; Furchi, M. M.; Bachmann, D.; Guider, R.; Fromherz, T.; Mueller, T. CMOS-Compatible Graphene Photodetector Covering All Optical Communication Bands. *Nat. Photonics* **2013**, *7*, 892−896.
(29) Youngblood, N.; Anugrah, Y.; Ma, R.; Koester, S. J.; Li, M. Multifunctional Graphene Optical Modulator and Photodetector Integrated on Silicon Waveguides. *Nano Lett.* **2014**, *14*, 2741−2746.
(30) Gan, X. T.; Shiue, R. J.; Gao, Y. D.; Meric, I.; Heinz, T. F.; Shepard, K.; Hone, J.; Assefa, S.; Englund, D. Chip-Integrated Ultrafast Graphene Photodetector with High Responsivity. *Nat. Photonics* **2013**, *7*, 883−887.
(31) Lin, H. T.; Song, Y.; Huang, Y. Z.; Kita, D.; Deckoff-Jones, S.; Wang, K. Q.; Li, L.; Li, J. Y.; Zheng, H. Y.; Luo, Z. Q.; Wang, H. Z.; Novak, S.; Yadav, A.; Huang, C. C.; Shiue, R. J.; Englund, D.; Gu, T.; Hewak, D.; Richardson, K.; Kong, J.; Hu, J. J. Chalcogenide Glass-on-Graphene Photonics. *Nat. Photonics* **2017**, *11*, 798−805.
(32) Mišeikis, V.; Marconi, S.; Giambra, M. A.; Montanaro, A.; Martini, L.; Fabbri, F.; Pezzini, S.; Piccinini, G.; Forti, S.; Terrés, B.; Goykhman, I.; Hamidouche, L.; Legagneux, P.; Sorianello, V.; Ferrari, A. C.; Koppens, F. H. L.; Romagnoli, M.; Coletti, C. Ultrafast, Zero-Bias, Graphene Photodetectors with Polymeric Gate Dielectric on Passive Photonic Waveguides. *ACS Nano* **2020**, *14*, 11190−11204.
(33) Guo, J. S.; Li, J.; Liu, C. Y.; Yin, Y. L.; Wang, W. H.; Ni, Z. H.; Fu, Z. L.; Yu, H.; Xu, Y.; Shi, Y. C.; Ma, Y. G.; Gao, S. M.; Tong, L. M.; Dai, D. X. High-Performance Silicon-Graphene Hybrid Plasmonic Waveguide Photodetectors beyond 1.55 μm. *Light: Sci. Appl.* **2020**, *9*, 29.
(34) Youngblood, N.; Chen, C.; Koester, S. J.; Li, M. Waveguide-Integrated Black Phosphorus Photodetector with Pigh Responsivity and Low Dark Current. *Nat. Photonics* **2015**, *9*, 247−252.
(35) Deckoff-Jones, S.; Lin, H. T.; Kita, D.; Zheng, H. Y.; Li, D. H.; Zhang, W.; Hu, J. J. Chalcogenide Glass Waveguide-Integrated Black Phosphorus Mid-Infrared Photodetectors. *J. Opt.* **2018**, *20*, 044004.
(36) Yin, Y.; Cao, R.; Guo, J.; Liu, C.; Li, J.; Feng, X.; Wang, H.; Du, W.; Qadir, A.; Zhang, H.; Ma, Y.; Gao, S.; Xu, Y.; Shi, Y.; Tong, L.; Dai, D. High-Speed and High-Responsivity Hybrid Silicon/Black-Phosphorus Waveguide Photodetectors at 2 μm. *Laser Photonics Rev.* **2019**, *13*, 1900032.
(37) Maiti, R.; Patil, C.; Saadi, M.; Xie, T.; Azadani, J. G.; Uluutku, B.; Amin, R.; Briggs, A. F.; Miscuglio, M.; Van Thourhout, D.; Solares, S. D.; Low, T.; Agarwal, R.; Bank, S. R.; Sorger, V. J. Strain-Engineered High-Responsivity $MoTe_2$ Photodetector for Silicon Photonic Integrated Circuits. *Nat. Photonics* **2020**, *14*, 578−584.
(38) Huang, L.; Dong, B. W.; Guo, X.; Chang, Y. H.; Chen, N.; Huang, X.; Liao, W. G.; Zhu, C. X.; Wang, H.; Lee, C.; Ang, K. W. Waveguide-Integrated Black Phosphorus Photodetector for Mid-Infrared Applications. *ACS Nano* **2019**, *13*, 913−921.
(39) Ma, P.; Flory, N.; Salamin, Y.; Baeuerle, B.; Emboras, A.; Josten, A.; Taniguchi, T.; Watanabe, K.; Novotny, L.; Leuthold, J. Fast $MoTe_2$ Waveguide Photodetector with High Sensitivity at Telecommunication Wavelengths. *ACS Photonics* **2018**, *5*, 1846−1852.
(40) Bie, Y. Q.; Grosso, G.; Heuck, M.; Furchi, M. M.; Cao, Y.; Zheng, J. B.; Bunandar, D.; Navarro-Moratalla, E.; Zhou, L.; Efetov, D. K.; Taniguchi, T.; Watanabe, K.; Kong, J.; Englund, D.; Jarillo-Herrero, P. A $MoTe_2$-Based Light-Emitting Diode and Photodetector for Silicon Photonic Integrated Circuits. *Nat. Nanotechnol.* **2017**, *12*, 1124−1129.
(41) Flory, N.; Ma, P.; Salamin, Y.; Emboras, A.; Taniguchi, T.; Watanabe, K.; Leuthold, J.; Novotny, L. Waveguide-Integrated van der Waals Heterostructure Photodetector at Telecom Wavelengths with High Speed and High Responsivity. *Nat. Nanotechnol.* **2020**, *15*, 118−124.
(42) Chen, W. J.; Khan, U.; Feng, S. M.; Ding, B. F.; Xu, X. M.; Liu, B. L. High-Fidelity Transfer of 2D Bi_2O_2Se and Its Mechanical Properties. *Adv. Funct. Mater.* **2020**, *30*, 2004960.
(43) Li, H.; Anugrah, Y.; Koester, S. J.; Li, M. Optical Absorption in Graphene Integrated on Silicon Waveguides. *Appl. Phys. Lett.* **2012**, *101*, 111110.
(44) Liu, Y.; Guo, J.; Zhu, E. B.; Liao, L.; Lee, S. J.; Ding, M. N.; Shakir, I.; Gambin, V.; Huang, Y.; Duan, X. F. Approaching the Schottky-Mott Limit in van der Waals Metal-Semiconductor Junctions. *Nature* **2018**, *557*, 696−700.
(45) Zhuo, L. Q.; Fan, P. P.; Zhang, S.; Liu, X. H.; Guo, X. Y.; Zhang, Y.; Zhan, Y. S.; Li, D. Q.; Che, Z.; Zhu, W. G.; Zheng, H. D.; Tang, J. Y.; Zhang, J.; Zhong, Y. C.; Luo, Y. H.; Yu, J. H.; Chen, Z. A Broadband All-Fiber Integrated Graphene Photodetector with CNT-Enhanced Responsivity. *Nanoscale* **2020**, *12*, 14188−14193.
(46) Assefa, S.; Xia, F. N.; Bedell, S. W.; Zhang, Y.; Topuria, T.; Rice, P. M.; Vlasov, Y. A. CMOS-Integrated High-Speed MSM Germanium Waveguide Photodetector. *Opt. Express* **2010**, *18*, 4986−4999.
(47) Yin, J. B.; Tan, Z. J.; Hong, H.; Wu, J. X.; Yuan, H. T.; Liu, Y. J.; Chen, C.; Tan, C. W.; Yao, F. R.; Li, T. R.; Chen, Y. L.; Liu, Z. F.; Liu, K. H.; Peng, H. L. Ultrafast and Highly Sensitive Infrared Photodetectors Based on Two-Dimensional Oxyselenide Crystals. *Nat. Commun.* **2018**, *9*, 3311.
(48) Hu, S. Q.; Zhang, Q.; Luo, X. G.; Zhang, X. T.; Wang, T.; Cheng, Y. C.; Jie, W. Q.; Zhao, J. L.; Mei, T.; Gan, X. T. Au-InSe van der Waals Schottky Junctions with Ultralow Reverse Current and High Photosensitivity. *Nanoscale* **2020**, *12*, 4094−4100.

https://doi.org/10.1021/acsnano.1c04359
ACS Nano XXXX, XXX, XXX−XXX

(49) Li, L.; Lin, H. T.; Huang, Y. Z.; Shiue, R. J.; Yadav, A.; Li, J. Y.; Michon, J.; Englund, D.; Richardson, K.; Gu, T.; Hu, J. J. High-Performance Flexible Waveguide-Integrated Photodetectors. *Optica* **2018**, *5*, 44−51.
(50) Goykhman, I.; Sassi, U.; Desiatov, B.; Mazurski, N.; Milana, S.; de Fazio, D.; Eiden, A.; Khurgin, J.; Shappir, J.; Levy, U.; Ferrari, A. C. On-Chip Integrated, Silicon-Graphene Plasmonic Schottky Photodetector with High Responsivity and Avalanche Photogain. *Nano Lett.* **2016**, *16*, 3005−3013.
(51) Ma, P.; Salamin, Y.; Baeuerle, B.; Josten, A.; Heni, W.; Emboras, A.; Leuthold, J. Plasmonically Enhanced Graphene Photodetector Featuring 100 Gbit/s Data Reception, High Responsivity, and Compact Size. *ACS Photonics* **2019**, *6*, 154−161.
(52) Gao, Y.; Zhou, G. D.; Tsang, H. K.; Shu, C. High-Speed van der Waals Heterostructure Tunneling Photodiodes Integrated on Silicon Nitride Waveguides. *Optica* **2019**, *6*, 514−517.
(53) Wang, Y.; Yu, Z. J.; Zhang, Z. Y.; Sun, B. L.; Tong, Y. Y.; Xu, J. B.; Sun, X. K.; Tsang, H. K. Bound-States-in-Continuum Hybrid Integration of 2D Platinum Diselenide on Silicon Nitride for High-Speed Photodetectors. *ACS Photonics* **2020**, *7*, 2643−2649.
(54) Ren, Y.; Van, V. Enhanced Small-Signal Responsivity in Silicon Microring Photodetector Based on Two-Photon Absorption. *IEEE J. Sel. Top. Quantum Electron.* **2020**, *26*, 3800208.
(55) Schuler, S.; Muench, J. E.; Ruocco, A.; Balci, O.; Thourhout, D. v.; Sorianello, V.; Romagnoli, M.; Watanabe, K.; Taniguchi, T.; Goykhman, I.; Ferrari, A. C.; Mueller, T. High-Responsivity Graphene Photodetectors Integrated on Silicon Microring Resonators. *Nat. Commun.* **2021**, *12*, 3733.
(56) Kita, T.; Tang, R.; Yamada, H. Compact Silicon Photonic Wavelength-Tunable Laser Diode with Ultra-Wide Wavelength Tuning Range. *Appl. Phys. Lett.* **2015**, *106*, 111104.
(57) Salleh, M. K. M.; Prigent, G.; Pigaglio, O.; Crampagne, R. Quarter-Wavelength Side-Coupled Ring Resonator for Bandpass Filters. *IEEE Trans. Microwave Theory Tech.* **2008**, *56*, 156−162.

https://doi.org/10.1021/acsnano.1c04359
ACS Nano XXXX, XXX, XXX−XXX